Study of the spontaneous magnetic phases in $TbIn_3$

1998 J. Phys.: Condens. Matter 10 3883

(http://iopscience.iop.org/0953-8984/10/17/018)

J. Phys.: Condens. Matter **10** (1998) 3883–3902. Printed in the UK PII: S0953-8984(98)90456-8

Study of the spontaneous magnetic phases in $TbIn_3$

R M Galéra†, M Amara†, P Morin† and P Burlet‡§

† Laboratoire Louis Néel‖, CNRS, BP 166, 38042 Grenoble Cédex 9, France

‡ Magnétisme et Diffraction Neutronique, DRF/MC, Centre d'Etudes Nucléaires, BP 85X, 38041 Grenoble Cédex, France

Received 7 January 1998

Abstract. The $AuCu_3$-type cubic compound, $TbIn_3$, undergoes below $T_N = 32$ K a spontaneous magnetic transition at $T_1 = 25$ K. The magnetic phase diagrams have been determined from the magnetization curves measured on a single crystal in fields up to 10 T. The corresponding magnetic structures have been determined from neutron diffraction studies on the same crystal under magnetic fields up to 5 T. For $T_1 < T < T_N$, the spin arrangement is commensurate, $\boldsymbol{q} = (1/2, 1/2, 0)$, and collinear with the spins pointing along a fourfold axis. At T_1, the structure remains commensurate, but becomes triple q, with the magnetic moments pointing along the threefold axes. The crystalline electric field (CEF) parameters have been deduced by analysing the magnetic and magnetostrictive properties of the $(Tb_{0.02}Y_{0.98})In_3$ dilute compound, within the CEF susceptibility formalism. Calculations within the mean-field approximation, taking account of CEF, bilinear and quadrupolar interactions, are presented, which describe quantitatively the properties of $TbIn_3$ in the low-field region.

1. Introduction

The complex magnetic properties of the rare-earth intermetallic compounds result from the competition between different types of interaction such as the crystalline electric field (CEF), RKKY-type bilinear exchange, quadrupolar interactions and magnetoelastic couplings [1]. In many rare-earth-based intermetallic systems, the long-range oscillatory character of the indirect exchange interactions tends to stabilize incommensurate magnetic structures, while the crystalline electric field determines the easy magnetization direction to be along a high-symmetry axis of the lattice. This gives rise to complex magnetic phase diagrams according to the temperature and the applied magnetic field [2, 3]. In high-symmetry systems, for instance the RAg and RCu compounds [4–6] which crystallize in the cubic CsCl-type structure, the competition between bilinear and quadrupolar interactions may stabilize non-commensurate magnetic structures and/or multiaxial magnetic structures. The case of DyAg is quite exemplary as it presents both types of ordering [7]. A modulated magnetic arrangement is stabilized just below the Néel temperature before the compound undergoes two successive magnetic transitions into double-q and triple-q commensurate structures. Though the quadrupolar interactions are generally dominated by the bilinear ones, they deeply influence the magnetic properties, as the nature of the magnetic transitions or the magnetic structure.

In the RIn_3 series which crystallize in the $AuCu_3$-type cubic structure the $NdIn_3$ and $TbIn_3$ compounds present magnetic properties very reminiscent of the RAg or RCu systems.

§ Member of the CNRS.

‖ Laboratory associated with the Université Joseph Fourier de Grenoble.

0953-8984/98/173883+20$19.50

In the antiferromagnetic domain both compounds present several spontaneous magnetic transitions [8, 9] as well as multistep magnetization processes. The magnetic properties of $NdIn_3$ have been intensively studied in the past three years [10–13]. The (H, T) magnetic phase diagrams have been determined along the three high-symmetry axes of the cubic structure. They reveal, in addition to the three spontaneous transitions, the existence of several field-induced phases. The spin arrangement in the different phases was investigated by neutron diffraction on a single crystal for the field along the [001] direction. In all the phases the magnetic moments are aligned along a fourfold axis. Concerning the spontaneous phases, just below $T_N = 5.9$ K, a sine-modulated structure stabilizes with a propagation vector $\boldsymbol{q}_1 = (1/2, 1/2, 0.036)$; the structure squares up at $T_1 = 5.08$ K with a new propagation vector, $\boldsymbol{q}_2 = (1/2, 1/2, 0.017)$. At $T_2 = 4.63$ K the structure becomes commensurate with $\boldsymbol{q} = (1/2, 1/2, 0)$. The spontaneous phases in $NdIn_3$ are all collinear. In contrast the field-induced phases at low temperatures remain commensurate, but present multi-q structures [11]. The collinear spin arrangement along the fourfold axis at zero field is in agreement with the easy axis imposed by the CEF interactions and the existence of positive quadrupolar interactions, as observed in the paramagnetic phase for the tetragonal symmetry [13]. The calculations of the free energy within a self-consistent periodic-molecular field model for both the dipolar and quadrupolar interactions allow one to reproduce the first-order character of the two spontaneous transitions and to predict the stabilization of multi-q structures by the applied field, keeping positive values of the quadrupolar interactions in the tetragonal symmetry.

$TbIn_3$ presents below $T_N = 32$ K a spontaneous phase transition at $T_1 = 25$ K. Previous studies at low temperatures have revealed multistep magnetization processes under high magnetic fields. At 4.2 K the first field-induced transition occurs for a critical field slightly higher than 10 T [8]. Czopnik *et al* [8] had calculated the free energy in $TbIn_3$, assuming negative values for the $A_4\langle r^4\rangle$ and $A_6\langle r^6\rangle$ CEF parameters. This hypothesis was based on the sign change of the CEF parameters from positive in $CeIn_3$ and $PrIn_3$ to negative in $NdIn_3$ as reported by Lethuillier and Chaussy [14]. They came to the conclusion that the spontaneous transition at T_1 is driven by the cross-over of degenerate crystal field levels in the molecular field, rejecting the stabilization of a multi-q structure below T_1. As the crystal field determines the 4f multiplet ground state of the rare earth, the determination of the CEF parameters is an essential step for the understanding of the magnetic properties. In cubic compounds the rare-earth ions are in high-symmetry positions and only the fourth and sixth CEF parameters, $A_4\langle r^4\rangle$, $A_6\langle r^6\rangle$, have to be considered. The recent study of the crystalline electric field in $NdIn_3$ by Amara *et al* [13] has shown that the actual CEF parameters in $NdIn_3$ are both positive ($A_4\langle r^4\rangle = +30.5$ K and $A_6\langle r^6\rangle = +6.8$ K) in contrast to the first determination by Lethuillier *et al* [14]. Positive CEF parameters in the Nd compound are in fair agreement with those found in $PrIn_3$ and $CeIn_3$ [14]. This is also much more consistent with the experimental fact that in all the other high-symmetry rare-earth intermetallics (CsCl, $AuCu_3$ or Laves phase structures) the $A_4\langle r^4\rangle$ parameter no longer changes sign when the rare earth varies from Ce to Yb [15]. Then the hypothesis of negative CEF parameters in the $TbIn_3$ compound appears questionable. The most direct technique for the determination of CEF parameters in cubic systems remains inelastic neutron spectroscopy. Unfortunately for $TbIn_3$, the inelastic spectra reveal very broad low-energy inelastic transitions ($\leqslant 40$ K) which cannot be unambiguously interpreted.

The CEF susceptibility formalism has been successfully applied to study the quadrupolar interactions in many rare-earth compounds [1]. This approach allows one to derive, within the perturbation theory in the paramagnetic range, an analytical expression for the four susceptibilities which couple the magnetization and the quadrupolar moment to the magnetic

field or stress. In the absence of bilinear and quadrupolar interactions their expressions are determined by the CEF level scheme only. Moreover the specific character of the low-lying CEF levels induces anisotropic behaviours, at least for the third-order magnetic susceptibility and the strain susceptibility. Then the CEF susceptibility formalism might be an alternative way to determine the CEF parameters in $TbIn_3$, by fitting the different experimental susceptibilities in a dilute compound. A similar analysis on yttrium-based rare-earth alloys has been performed in the past to determine the CEF parameters of rare-earth ions from magnetic measurements [16, 17].

We present in this paper a study of the spontaneous magnetic phases in $TbIn_3$. The CEF susceptibility formalism and the expression of the CEF susceptibilities deduced in absence of any pair interaction are presented in section 2. Section 3 concerns the experimental details of the magnetization, magnetostriction and neutron diffraction measurements. The results of magnetization and neutron diffraction experiments on the concentrated compound $TbIn_3$ are reported in section 4. Section 5 is devoted to the determination of the CEF parameters by analysing the magnetic and magnetostrictive properties of the dilute compound $(Tb_{0.02}Y_{0.98})In_3$, within the CEF susceptibility formalism. Finally, in section 6, we present calculations performed within the periodic-molecular field approach which takes into account the CEF, bilinear and quadrupolar interactions in order to describe quantitatively the magnetic properties of $TbIn_3$.

2. CEF susceptibility formalism

The magnetic properties of the 4f shell are usually described using the Hamiltonian:

$$\mathcal{H} = \mathcal{H}_{CEF} + \mathcal{H}_J + \mathcal{H}_{ME} + \mathcal{H}_Q. \tag{1}$$

$\mathcal{H}_{CEF}$ is the usual crystalline electric field Hamiltonian, the terms of which are written using the Stevens' operator equivalents method. For a cubic symmetry, it is expressed in the fourfold axis system as:

$$\begin{aligned} \mathcal{H}_{CEF} &= A_4\langle r^4\rangle B_J O_4 + A_6\langle r^6\rangle \gamma_J O_6 \\ \mathcal{H}_{CEF} &= \frac{Wx}{F_4}(O_4^0 + 5O_4^4) + \frac{W(1-|x|)}{F_6}(O_6^0 - 21O_6^4). \end{aligned} \tag{2}$$

W and x are the usual CEF parameters introduced by Lea *et al* [18].

$\mathcal{H}_J$ describes the Zeeman coupling and the Heisenberg exchange interaction acting on a given site i:

$$\mathcal{H}_J = -g_J\mu_B(\boldsymbol{H} + \boldsymbol{H}_{ex})\cdot \boldsymbol{J}_i \qquad \boldsymbol{H} = \boldsymbol{B}/\mu_0. \tag{3}$$

$\boldsymbol{H}_{ex}$ is the exchange molecular field. In the paramagnetic range it is given by:

$$\boldsymbol{H}_{ex} = ng_J\mu_B\langle J\rangle = \frac{J(0)}{g_J\mu_B}\langle \boldsymbol{J}\rangle. \tag{4}$$

n is the isotropic paramagnetic bilinear exchange parameter. n is proportional to the Fourier transform $J(\boldsymbol{k})$ of the pair interaction coupling constant $J(\boldsymbol{R}_j)$ at $\boldsymbol{q} = \boldsymbol{0}$:

$$J(\boldsymbol{k}) = \sum_{j\neq i} J(\boldsymbol{R}_i)\, \mathrm{e}^{\mathrm{i}\boldsymbol{k}\cdot\boldsymbol{R}_j}. \tag{5}$$

In the ordered range the periodic-field formalism has been recently developed [19, 20] to take into account the magnetic periodicity. Within this approach the expression of the exchange field is:

$$\boldsymbol{H}_{ex}(\boldsymbol{R}_i) = \sum_k J(\boldsymbol{k})\boldsymbol{m}_k \, \mathrm{e}^{\mathrm{i}k\boldsymbol{R}_i}. \tag{6}$$

$\boldsymbol{m}_k$ is the Fourier component of the magnetic moment propagated by $\boldsymbol{k}$.

$\mathcal{H}_{ME}$ is the one-ion magnetoelastic Hamiltonian

$$\mathcal{H}_{ME} = -B^{\gamma}(\varepsilon_1^{\gamma} O_2^0 + \sqrt{3}\varepsilon_2^{\gamma} O_2^2) - B^{\varepsilon}(\varepsilon_1^{\varepsilon} P_{xy} + \varepsilon_2^{\varepsilon} P_{yz} + \varepsilon_3^{\varepsilon} P_{zx}) \tag{7}$$

it takes into account only the strain modification of the CEF second-order term. High-order modifications and two-ion magnetoelastic couplings are neglected. B^{γ}, B^{ε} are the magnetoelastic parameters associated with the tetragonal, ε^{γ}, and trigonal, $\varepsilon^{\varepsilon}$, strain modes, respectively.

$\mathcal{H}_Q$ is the quadrupolar Hamiltonian. As the Heisenberg exchange interaction it is treated within the mean-field approximation. In the periodic-field approach it is expressed by:

$$\mathcal{H}_Q = -Q_{O_2^0}(\boldsymbol{R}_i)O_{2i}^0 - 3Q_{O_2^2}(\boldsymbol{R}_i)O_{2i}^2 - Q_{P_{xy}}(\boldsymbol{R}_i)P_{xyi} - Q_{P_{yz}}(\boldsymbol{r}_i)P_{yzi} - Q_{P_{zx}}(\boldsymbol{R}_i)P_{zxi} \tag{8}$$

the $Q_{O_l^m}(\boldsymbol{R}_i)$ and $Q_{P_{\alpha\beta}}(\boldsymbol{R}_i)$ terms represent the quadrupolar fields associated with each quadrupolar component. For instance in the tetragonal symmetry

$$Q_{O_2^0}(\boldsymbol{R}_i) = \sum_k K^{\gamma}(\boldsymbol{k})\mathcal{O}_{2k}^0 \, \mathrm{e}^{\mathrm{i}\boldsymbol{k}\cdot\boldsymbol{R}_i}. \tag{9}$$

$\mathcal{O}_{2k}^0$ is a Fourier quadrupolar component of $\langle O_2^0 \rangle$ and $K^{\gamma\varepsilon}(\boldsymbol{k})$ the Fourier transforms of the quadrupolar pair coefficients associated with the tetragonal (γ) and trigonal (ε) symmetries. $K^{\gamma\varepsilon}(\boldsymbol{k})$ are analogous to $J(\boldsymbol{k})$ for the bilinear interactions. In the paramagnetic range this leads to:

$$\mathcal{H}_Q = -K^{\gamma}(0)[\langle O_2^0 \rangle O_2^0 + 3\langle O_2^2 \rangle O_2^2] - K^{\varepsilon}(0)[\langle P_{xy} \rangle P_{xy} + \text{cycl.}]. \tag{10}$$

The paramagnetic phase can be described using the perturbational treatment of the total Hamiltonian (1). An expansion, carried out up to the fourth order in $\boldsymbol{H}$ and to the second order in $\varepsilon^{\gamma,\varepsilon}$ allows one to obtain the partition function Z and the free energy $F^{\gamma,\varepsilon}$. For instance, in the case of the tetragonal symmetry, the total energy is expressed as:

$$\begin{aligned} F^{\gamma} = F_{CEF}^0 &- \tfrac{1}{2}\chi_0(\boldsymbol{H} + n\boldsymbol{M})^2 - \tfrac{1}{2}\chi_{\gamma}(B^{\gamma}\varepsilon_1^{\gamma} + K^{\gamma}Q)^2 - \chi_{\gamma}^{(2)}(\boldsymbol{H} + n\boldsymbol{M})^2(B^{\gamma}\varepsilon_1^{\gamma} + K^{\gamma}Q) \\ &- \tfrac{1}{4}\chi_{\gamma}^{(3)}(\boldsymbol{H} + n\boldsymbol{M})^4 + \cdots \end{aligned} \tag{11}$$

where F_{CEF}^0 is the zeroth-order energy corresponding to $\mathcal{H}_{CEF}$ alone. The four CEF single-ion susceptibilities, used in the expression (11), depend on the CEF scheme and on the matrix elements of the dipolar, $\boldsymbol{J}$, and quadrupolar, O_2^0, operators. The equilibrium values of $\boldsymbol{M}$, $Q = \langle O_2^0 \rangle$ and ε are deduced from the minimization of the free energy.

In the absence of any pair interactions ($n \equiv K^{\mu} \equiv 0$) this leads to:

$$\begin{aligned} &\boldsymbol{M} = \chi_0\boldsymbol{H} + \chi_{0\mu}^{(3)}\boldsymbol{H}^3 \qquad (\mu = \gamma, \varepsilon) \\ &Q = \chi_Q\boldsymbol{H}^2 \end{aligned} \tag{12}$$

and in the tetragonal symmetry

$$\varepsilon_1^{\gamma} = \frac{B^{\gamma}}{C_0^{\gamma}}Q = \frac{B^{\gamma}}{C_0^{\gamma}}\chi_Q\boldsymbol{H}^2 \qquad \chi_Q = \frac{\chi_{\gamma}^{(2)}}{1 - [(B^{\gamma})^2/C_0^{\gamma}]\chi_{\gamma}} \tag{13}$$

or in the trigonal symmetry

$$\varepsilon^{\varepsilon} = \varepsilon_1^{\varepsilon} = \varepsilon_2^{\varepsilon} = \varepsilon_3^{\varepsilon} = \frac{B^{\varepsilon}}{C_{\varepsilon}^0}P = \frac{B^{\varepsilon}}{C_{\varepsilon}^0}\chi_P\boldsymbol{H}^2 \qquad \chi_P = \frac{\chi_{\varepsilon}^{(2)}}{1 - 3[(B^{\varepsilon})^2/C_0^{\varepsilon}]\chi_{\varepsilon}}. \tag{14}$$

χ_0 and $\chi_{0\mu}^{(3)}$ are the first and third-order magnetic susceptibilities. χ_Q and χ_P are the total quadrupolar susceptibilities for a tetragonal and trigonal mode respectively. They are expressed as functions of the strain susceptibility, χ_μ, and the quadrupolar field susceptibility, $\chi_\mu^{(2)}$. The C_0^μ are the symmetrized background elastic constants in the absence of magnetic contributions.

In the absence of dipolar and quadrupolar interactions, the behaviour of all the susceptibilities is only governed by the crystalline electric field. Depending on the low-lying levels, the first-order magnetic susceptibility may have different curvatures. In the same way the third-order and quadrupolar field susceptibilities may be anisotropic. All these effects are selective in the experimental determination of the CEF scheme and very complementary to the neutron scattering measurements.

The analysis of the magnetization curves provides the experimental determination of the first- and third-order susceptibilities. In the present work the quadrupolar field susceptibility $\chi_{Q,P}$ is deduced from the parastriction measurements. The change of length induced by an applied field is given by [19]:

$$\frac{\mathrm{d}l}{l} = \lambda_{\beta_1\beta_2\beta_3} = \frac{\varepsilon^\alpha}{\sqrt{3}} + \frac{\varepsilon_1^\gamma}{\sqrt{6}} - (2\beta_3^2 - \beta_1^2 - \beta_2^2) + \frac{\varepsilon_2^\gamma}{\sqrt{2}}(\beta_1^2 - \beta_2^2) + \sqrt{2}(\varepsilon_1^\varepsilon\beta_1\beta_2 + \varepsilon_2^\varepsilon\beta_2\beta_3 + \varepsilon_3^\varepsilon\beta_3\beta_1). \tag{15}$$

β_i $(i = 1, 2, 3)$ are the direction cosines of the direction of the measurements. In order to eliminate the volume effects ε^α, the relative change of the length is usually measured successively parallel $(\lambda_\parallel)$ and perpendicular $(\lambda_\perp)$ to the field direction. As a consequence, for a magnetic field along the fourfold or threefold directions and according to (14) and (15), one obtains respectively:

$$(\lambda_\parallel - \lambda_\perp)_\gamma = \sqrt{\frac{3}{2}}\frac{B^\gamma}{C_0^\gamma}\chi_Q \boldsymbol{H}^2 \qquad (\lambda_\parallel - \lambda_\perp)_\varepsilon = \frac{3}{\sqrt{2}}\frac{B^\varepsilon}{C_0^\varepsilon}\chi_P \boldsymbol{H}^2 \tag{16}$$

or in a linearized representation:

$$\frac{H}{\sqrt{|\lambda_\parallel - \lambda_\perp|_\gamma}} = \left(\frac{2}{3}\right)^{1/4}\left(\frac{C_0^\gamma}{B^\gamma}\right)^{1/2}\chi_Q^{-1/2}$$
$$\frac{H}{\sqrt{|\lambda_\parallel - \lambda_\perp|_\varepsilon}} = \left(\frac{\sqrt{2}}{3}\right)^{1/2}\left(\frac{C_0^\varepsilon}{B^\varepsilon}\right)^{1/2}\chi_P^{-1/2}. \tag{17}$$

The high-temperature slope of $H/\sqrt{|\lambda_\parallel - \lambda_\perp|}$ gives the magnetoelastic coefficient B^μ.

3. Experimental conditions

The single crystals of $TbIn_3$ and $(Tb_{0.02}Y_{0.98})In_3$ were prepared using the Bridgman technique in tantalum crucibles. The purity of the components was 4 N for Tb and 5 N for In. A 4 N ingot of yttrium has been purified for one month at 1200 °C using a solid state electrolysis technique. The ratio, $\rho_{300}/\rho_{4.2}$, between the resistivity at 300 K and 4.2 K of the purified yttrium ingot is higher than 100. Part of this ingot was used for the preparation of a single crystal of the dilute compound. For this compound the masses of the components were adjusted to obtain a Tb concentration close to 2%. The rest of the purified yttrium ingot was used for the preparation of a polycrystalline YIn_3 alloy. A spherical sample of 5 mm diameter was spark-cut from the monocrystalline ingot of $TbIn_3$. This sample was used for both the magnetization and the neutron diffraction experiments.

From the $(Tb_{0.02}Y_{0.98})In_3$ ingot, two cylindrical samples were spark-cut, one ($h = 6.67$ mm, $\phi = 6.33$ mm) with h parallel to the [001] axis of the $AuCu_3$ structure and a second one ($h = 4.84$ mm, $\phi = 6.35$ mm) with h parallel to the [111] axis.

Magnetization measurements have been performed at the Laboratoire Louis Néel by the extraction method in a cryomagnet which supplies magnetic fields up to 10 T in the temperature range 1.5–300 K. The accuracy of the magnetic measurements is better than 10^{-3} μ_B/atom.

In the ordered phase of $TbIn_3$ the isothermal magnetization processes were measured with the field applied successively along the [001], [110] and [111] directions of the cubic structure. Along the [001] and [111] axes, measurements were performed only in fields up to 7.5 T. We mainly focused here on measurements along the [110] axis, as this symmetry was kept for the neutron diffraction experiments. Along this direction, magnetization measurements were performed up to 10 T. Isofield magnetization curves were performed with the field applied along the [001] and [110] directions. In the paramagnetic phase magnetization curves were measured up to 300 K with the field applied along the [001] direction.

In the dilute Tb compound isothermal magnetization curves have been measured with the field applied along the [001] and [111] directions using the two cylindrical samples in the temperature range 1.5–300 K. Measurements with the field along the fourfold axis have been performed down to 100 mK using a dilution refrigerator.

The first-order magnetic susceptibility in $(Tb_xY_{1-x})In_3$, YIn_3 and in the paramagnetic domain of $TbIn_3$ was deduced from Arrott plots and $M/H = f(H^2)$ curves. Figure 1 displays the Arrott plots of the dilute compound where the magnetization in μ_B units is deduced assuming the nominal Tb concentration of 2%. The susceptibilities of the Tb compounds were first corrected from the matrix contribution using the YIn_3 susceptibility. The YIn_3 susceptibility (figure 2) contains the Pauli and diamagnetic contributions of the matrix and the paramagnetic behaviour of the impurities. All these contributions become important when the magnetism is weak e.g. in the dilute compound or at high temperatures in the concentrated one: $\chi_{corr}(T) = \chi_{meas}(T) - \chi_{YIn_3}(T)$.

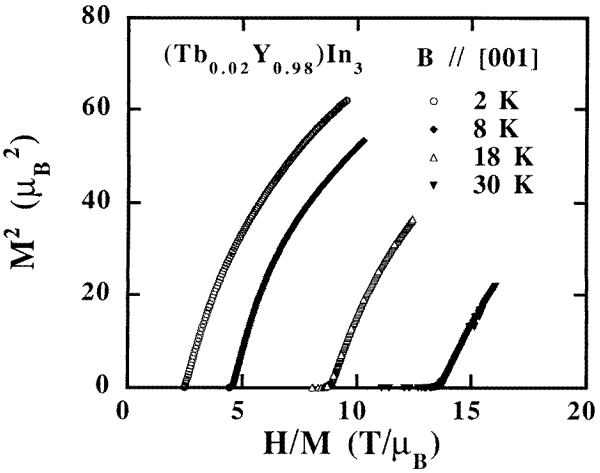

Figure 1. Arrott plots obtained from isothermal magnetization curves in $(Tb_{0.02}Y_{0.98})In_3$ for a magnetic field applied along the [001] axis.

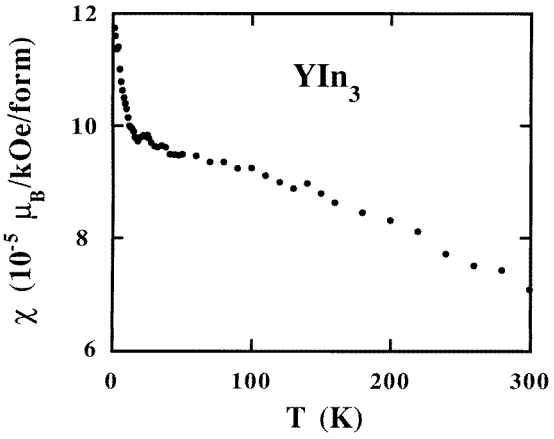

Figure 2. First-order magnetic susceptibility of the high-purity polycrystalline sample of YIn_3.

For the dilute compound the Curie constant deduced from the slope at high temperature of $1/\chi_{corr}$ confirms a Tb^{3+} ion concentration very close to 2%. In order to obtain the susceptibility per Tb ion in this compound the data were further corrected from the concentration x : $\chi_{CEF} = (1/x)\chi_{corr}$.

The third-order magnetic susceptibility was deduced from the slope of the linear part of both the Arrott plots and the $M/H = f(H^2)$ curves. In this case no matrix correction was performed as no significant deviation is observed in the magnetization curves of YIn_3. For the dilute compound, the third-order magnetic susceptibility by Tb ion is obtained, as for the first-order one, after correction for the concentration.

Magnetostriction measurements on the two dilute samples were performed using two electrical strain gauges mounted in a Wheastone bridge. The active gauge is glued on the sample along a given crystallographic axis. The field-induced change length is measured with the magnetic field applied successively parallel and perpendicular to it. A second one, glued on a high-purity copper sample with the same orientation, is used as reference. Measurements were performed in magnetic fields up to 5 T with a relative accuracy of about 10^{-7}.

The thermal variation of $H/\sqrt{|\lambda_\parallel - \lambda_\perp|}$ was determined for both the tetragonal ($H \parallel \langle 001 \rangle$) and trigonal ($H \parallel \langle 111 \rangle$) modes from the magnetostriction measurements. The value of $\lambda_\parallel - \lambda_\perp$ is observed to be negative for both modes. Assuming, as usually done [20], that the measured macroscopic deformation of the crystal depends linearly on the concentration, we have then from (17) that in the dilute compound $H/\sqrt{|\lambda_\parallel - \lambda_\perp|}_\mu \approx (xB^\mu)^{-1/2}\chi_{Q,P}^{-1/2}$, with x the rare-earth concentration. The results have been then corrected according to this expression.

Neutron diffraction experiments have been carried out on the DN3 spectrometer, at the CEN Grenoble reactor, SILOE. A cryomagnet supplies a vertical magnetic field up to 6 T in the temperature range 1.5 to 300 K. The moving up counter allows us to perform scans out of the equatorial reciprocal plane, inside the limits imposed by the magnet aperture (-5° to 10°). The selected wavelength of the incident beam is $\lambda = 1.537$ Å. The $\lambda/2$ harmonic contamination has been checked to be less than $1‰$ in the diffracted intensities. The spherical shape of the sample leads to an absorption coefficient constant for

all the reflections. Then despite the large absorption cross section of indium no absorption corrections have been performed. The sample was mounted with the $[1\bar{1}0]$ twofold axis vertical (the $[1\bar{1}0]$ axis is parallel to the direction of the applied field) and lined up in the paramagnetic phase using the main nuclear Bragg reflections of the $AuCu_3$ structure at $T = 38$ K in zero field. To avoid magnetoremanent effects when the field is applied, at each value of the field the sample was first warmed up above T_N, before cooling down to the temperature of the measurement. Up to 58 reflections were collected in fields of 0, 1.5 and 5 T at 28 K and 24 K. At 4.8 K measurements were also performed under a field of 5 T.

4. The concentrated compound: $TbIn_3$

4.1. Magnetization measurements

Figure 3(a) shows the magnetization curves measured at 4 K along the three high-symmetry axes of the cube. The magnetization presents no anisotropy up to 4 T. In field larger than 4 T, the magnetization along the [111] axis becomes larger than that along the two other axes. This feature is in agreement with results of Czopnik *et al* [8]. The steep rise of the magnetization along [110], just below 10 T, indicates the beginning of the first field-induced

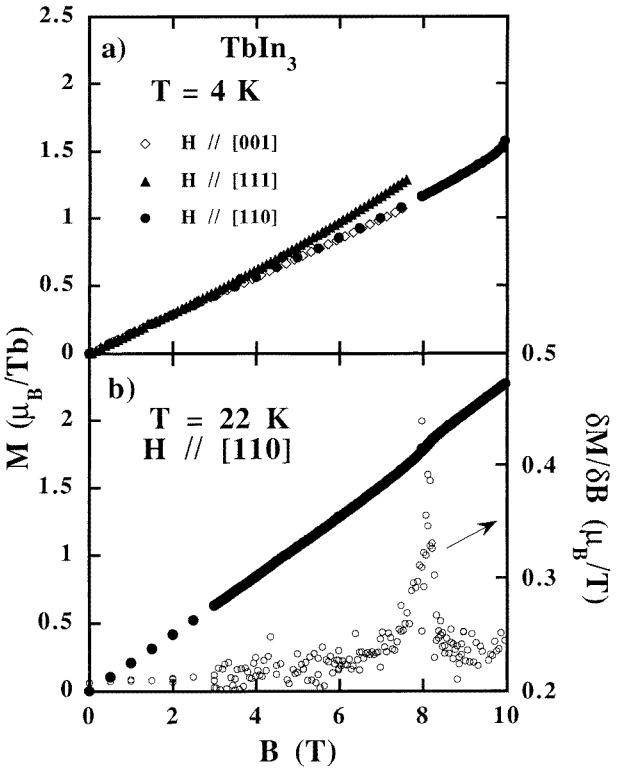

Figure 3. (a) Magnetization processes at 4 K in $TbIn_3$ along the three high-symmetry axes of the cubic structure. (b) Magnetization curve at 22 K in $TbIn_3$ for a field applied along the twofold axis (full dots) and field derivative of the curve (open dots).

transition, which was observed at a critical field slightly larger than 10 T. Along the [001] and [111] axes, no anomaly is observed in the whole ordered domain for applied field less than 7.5 T. When the temperature is increased the jump in the [110] magnetization rapidly vanishes. A very smooth jump is observed again at 21 K. The value of the critical field determined by the maximum of the derivative $\delta M/\delta B$ is $\mu_0 H_c = 9$ T. The critical field rapidly decreases with the temperature; for instance at 22 K the critical field is only 8 T (see figure 3(b)). At 26 K no more singularities appear in the magnetization curves. For higher temperatures the magnetization along the three axes behaves linearly with the field.

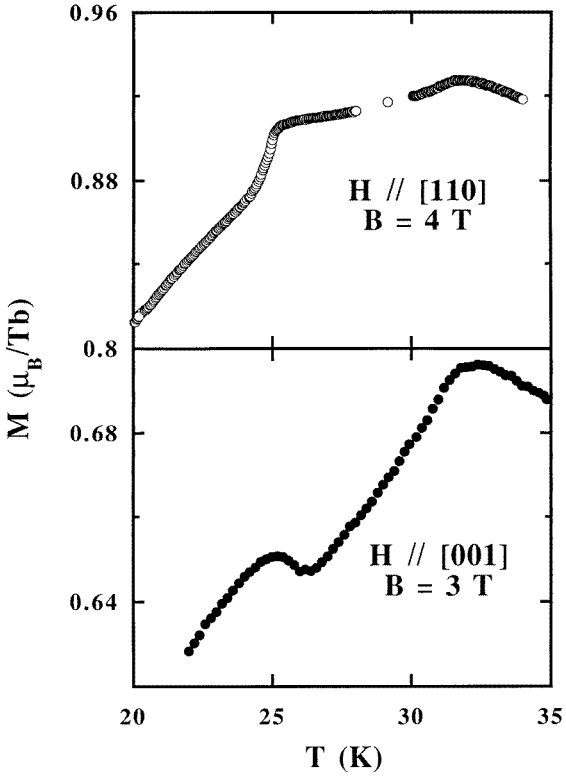

Figure 4. Isofield magnetization curves in $TbIn_3$ measured for an applied field of 3 T applied along the [001] axis and for a field of 4 T applied along the [110] axis.

In the $M(T)$ curves the transition at T_N corresponds to a maximum. When the field is applied along the [001] axis, the isofield curves present a well pronounced minimum as shown in figure 4. The temperature at which the minimum is observed is taken as the transition temperature T_1. This transition has been followed in fields up to 7 T. Along the [110] axis the minimum in the $M(T)$ curves is only observed under weak applied fields. In higher fields the transition is evidenced by an abrupt change in the slope of the curve (figure 4). The (H, T) magnetic phase diagram determined in the low-field region for the field along [001] presents almost vertical transition lines at T_N and T_1 (figure 5). For fields parallel to the [110] axis the transition line at T_N remains also vertical up to 8 T (figure 5). The transition line at T_1, deduced from both isothermal and isofield curves, presents a more pronounced curvature.

The thermal variation of the inverse of the first-order magnetic susceptibility of $TbIn_3$ is presented in figure 6. It varies linearly with the temperature from 50 to 300 K and intercepts

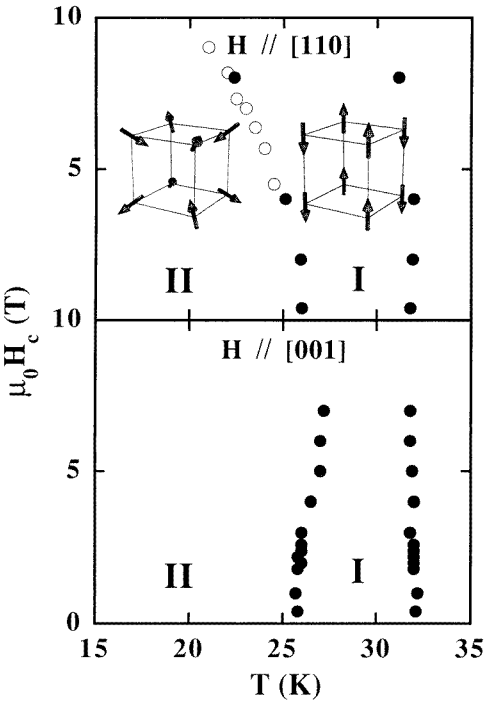

Figure 5. Magnetic phase diagrams of $TbIn_3$ determined in the low-field region for applied fields along the [001] and [110] axes. Full dots represent the transitions observed in isofield magnetization curves. Open dots represent the transitions observed in isothermal magnetization processes. The insets represent the non-distorted magnetic structures obtained from neutron diffraction experiments in the two spontaneous magnetic phases.

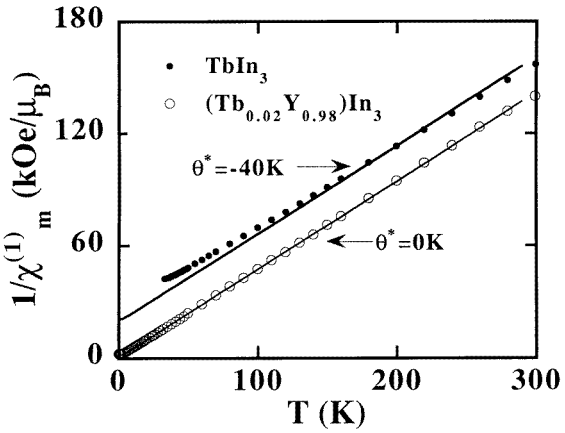

Figure 6. Thermal variation of the inverse of the first-order magnetic susceptibility in $TbIn_3$ (full dots) and $(Tb_{0.02}Y_{0.98})In_3$ (open dots). The data have been all corrected from the matrix contributions. The full lines represent the variations calculated with the set of CEF parameters: $W = -0.31$ K and $x = -0.89$. The best fit in $TbIn_3$ (full line) is obtained with the bilinear exchange coefficient $\theta^* = -40$ K.

the temperature axis at $T = -56 \pm 1$ K. This gives us a first evaluation of the paramagnetic bilinear exchange parameter. Below 50 K a small curvature is observed which very likely arises from short range order effects. Indeed in the course of preliminary powder neutron diffraction studies [21], the pattern collected at 40 K in $TbIn_3$ revealed a broad bump centred around the 2θ position of the $(1/2, 1/2, 0)$ magnetic satellites. Such bumps are generally due to short-range magnetic correlations in the paramagnetic phase. The effective moment determined from the slope of $1/\chi = f(T)$, $\mu_{effec} = 10.1 \pm 0.05\ \mu_B$, is 4% larger than the free Tb^{3+} ion value, 9.721 μ_B. The magnitude of the third-order magnetic susceptibility is observed to be smaller than the experimental sensitivity in the whole paramagnetic range.

4.2. Neutron diffraction results

A first collection of integrated intensities at $T = 38$ K and zero field gave a determination of the $\lambda/2$ harmonic contamination and the background at the magnetic satellite positions. The refinement of the integrated intensities is in a satisfactory agreement with the $AuCu_3$ structure (the reliability factor $R = 7\%$). Cooling down the sample, magnetic satellites start to rise below $T_N = 32$ K at the positions expected for propagation vectors belonging to the $\langle 1/2, 1/2, 0\rangle$ star. The thermal evolution of the intensity at the $(1/2, 1/2, 0)$ node of the reciprocal space was followed down to 20 K. This evolution clearly presents a discontinuity at 26 K, a temperature which corresponds to the transition in phase II in the magnetic phase diagram (figure 5). In a first step the evolution with the magnetic field of the intensity of the $(1/2, 1/2, 0)$, $(1/2, 0, 1/2)$ and $(0, -1/2, 1/2)$ reflections was checked at 28 K in phase I. At zero field the three reflections have roughly the same intensity. Increasing the field the $(1/2, 0, 1/2)$ and $(0, -1/2, 1/2)$ intensities rapidly fall, while the $(1/2, 1/2, 0)$ one increases. Such an evolution is distinctive of the domain motion in a single-q antiferromagnetic spin arrangement. Under an applied field of 5 T the thermal evolution of the intensity of the three satellites has been followed cooling down the sample. This evolution, presented in figure 7, confirms a single q-arrangement in phase I. At the transition in phase II, the intensities of both the $(0, -1/2, 1/2)$ and the $(1/2, 0, 1/2)$ reflections steeply increase while the $(1/2, 1/2, 0)$ one decreases. This behaviour is characteristic of a transition towards a multi-q magnetic structure. Moreover

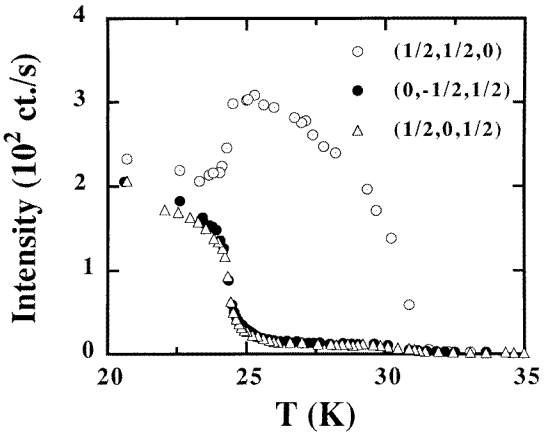

Figure 7. Thermal variation of the intensity of the $(1/2, 1/2, 0)$, $(1/2, 0, 1/2)$ and $(0, -1/2, 1/2)$ magnetic satellites under an applied field of 5 T.

the fact that the three reflections approximately recover the same intensity in phase II is strongly consistent with a triple-q structure.

The models of spontaneous magnetic structures for a propagation vector belonging to the $\langle 1/2, 1/2, 0\rangle$ star and where the magnetic moments satisfy the two conditions (i) constant modulus on all the magnetic sites and (ii) easy direction frozen by the CEF along one family of high-symmetry axes have been listed by Morin and Schmitt [5]. These structures can also be deduced by analogy from the inventory of the high-symmetry magnetic structures with $q \in \langle 1/2, 0, 0\rangle$ star given more recently in [22]. The analysis of the data was performed using a least-squares procedure. For each model of magnetic structure the program determines the different domains and adjusts their relative proportions, as well as the amplitude of the magnetic moment. The reliability factor is defined by:

$$R = \left(\sum_i^{n_{obs}} p_i |I^i_{cal} - I^i_{obs}| / I^i_{obs} \right) \Big/ \sum_i^{nobs} p_i$$

n_{obs} is the number of the observed reflections and p_i the weight of the reflection i. p_i corresponds to the inverse of the statistical error of the intensity I^i_{obs}.

The refinements in phase II give the best agreement for a three-q structure with the spins aligned along a threefold axis. When $B \neq 0$, it is necessary to take into account a distortion of the magnetic structure induced by the field. This is the case in particular when the CEF anisotropy is weak and/or at high temperatures. Such a distortion is in agreement with a non-negligible susceptibility observed in the magnetization curves (see figure 3). The non-distorted structure which gives the best agreement is described by the following Fourier components:

$$\begin{aligned} \boldsymbol{M}_{\boldsymbol{q}_1} &= (0, 0, 1/\sqrt{3}) \qquad \text{with } \boldsymbol{q}_1 = (1/2, 1/2, 0) \\ \boldsymbol{M}_{\boldsymbol{q}_2} &= (1/\sqrt{3}, 0, 0) \qquad \text{with } \boldsymbol{q}_2 = (0, 1/2, 1/2) \\ \boldsymbol{M}_{\boldsymbol{q}_2} &= (0, 1/\sqrt{3}, 0) \qquad \text{with } \boldsymbol{q}_3 = (1/2, 0, 1/2). \end{aligned}$$

Taking into account the distortion, the magnetic moment in Bohr magnetons is then given by:

$$\boldsymbol{M}(\boldsymbol{r}_i) = M \sum_{\boldsymbol{q}_j} \boldsymbol{M}_{\boldsymbol{q}_j} \cos(2\pi \boldsymbol{r}_i \cdot \boldsymbol{q}_j) + \boldsymbol{M}_0 \qquad \text{with } \boldsymbol{M}_0 = F(1/\sqrt{2}, -1/\sqrt{2}, 0).$$

Table 1. Refined values of the parameters M and F obtained for the triple-q structure model in phase II of the (H, T) magnetic phase in $TbIn_3$. The structure is defined by the Fourier components:

$$\begin{aligned} \boldsymbol{M}_{\boldsymbol{q}_1} &= (0, 0, 1/\sqrt{3}) \qquad \text{with } \boldsymbol{q}_1 = (1/2, 1/2, 0) \\ \boldsymbol{M}_{\boldsymbol{q}_2} &= (1/\sqrt{3}, 0, 0) \qquad \text{with } \boldsymbol{q}_2 = (0, 1/2, 1/2) \\ \boldsymbol{M}_{\boldsymbol{q}_3} &= (0, 1/\sqrt{3}, 0) \qquad \text{with } \boldsymbol{q}_3 = (1/2, 0, 1/2). \end{aligned}$$

For each site the magnetic moment is given by:

$$\boldsymbol{M}(\boldsymbol{r}_i) = M \sum_{\boldsymbol{q}_j} \boldsymbol{M}_{\boldsymbol{q}_j} \cos(2\pi \boldsymbol{r}_i \cdot \boldsymbol{q}_j) + \boldsymbol{M}_0 \qquad \text{with } \boldsymbol{M}_0 = F(1/\sqrt{2}, -1/\sqrt{2}, 0).$$

The reliability factor obtained for each refinement is given in row 5.

$\mu_0 H$ (T)	T (K)	M (μ_B)	F (μ_B)	R (%)
0	24	5.98	0	9.7
1.5	24	5.99	0.07	10.7
5	24	5.65	0.18	12.5
5	4.8	7.63	0.08	11.3

Table 2. Refined values of the parameters M, F and domain proportions d_1, d_2 and d_3 obtained at 28 K for the collinear structure model in phase I of the (H, T) magnetic phase diagram in $TbIn_3$. The magnetic moment is given by:
$\boldsymbol{M}(\boldsymbol{r}_i) = M\boldsymbol{M}_q \cos(2\pi \boldsymbol{r}_i \cdot \boldsymbol{q}) + \boldsymbol{M}_0$ with $\boldsymbol{M}_0 = F(1/\sqrt{2}, -1/\sqrt{2}, 0)$.
The reliability factor obtained for each refinement is given in row 6.

$\mu_0 H$ (T)	M (μ_B)	F (μ_B)	d_1 (%)	d_2 (%)	d_3 (%)	R (%)
0	4.81	0	32.3	35.3	32.4	9
1.5	4.87	0.09	50.4	25.6	9.5	9.5
5	4.59	0.23	92.2	4.0	3.8	13.9

Table 3. Integrated intensities observed at 4.8 and 28 K under an applied field of 5 T and calculated intensities obtained for triple-q and single-q structures.

	$T = 4.8$ K (triple-q)			$T = 28$ K (single q)		
h, k, l	I_{obs}	I_{cal}	p_i	I_{obs}	I_{cal}	p_i
1/2, 1/2, 0	280	280.9	100	249	292	50
1/2, 0, 1/2	234	280.9	101	10.8	11.3	25
1/2, 0, −1/2	272	280.9	106	11.5	11.3	25
0, −1/2, 1/2	261	280.9	101	11.9	11.9	20
0, −1/2, −1/2	254	280.9	103	11	11.9	20
1/2, 1/2, 1	103	79.4	59	88.7	82.6	50
−1/2, −1, 1/2	95.7	79.4	60	3.4	3.2	6
−1/2, −1, −1/2	95.4	79.4	61	3.5	3.2	6
1, 1/2, 1/2	80.8	79.4	56	2.5	3.4	5
1/2, 0, 3/2	211	205.7	73	10.7	8.3	13
0, −1/2, 3/2	232	205.7	74	12.3	8.8	10
3/2, 1, 1/2	123	128	50	3.2	5.2	2
−1/2, −1, 3/2	151	128	50	2.7	5.2	2
1, 1/2, 3/2	127	128	51	4.9	5.5	4
1/2, 1/2, 2	24.3	17.5	15	19.4	18.2	13
3/2, 3/2, 2	52.7	54.8	44	46.8	57	50
−3/2, −2, −3/2	55.9	54.8	34	3.5	2.2	5
1/2, 1/2, 3	7	5	4	4.6	5.2	3
−2, −5/2, 1/2	45.2	53.1	12	1.9	2.3	1
1, 1, 0	29.7	29.5	42	37.3	37.2	50
−1, −2, 0	31	27.7	24	32.9	32.2	25
−1, −2, 1	20.5	27.5	20	23.9	31.5	20

In this model, the structure is single domain. It should be noted that in the distorted structure the modulus of the magnetic moment becomes site dependent. The refined values of M and F and the associated reliability factors are given in table 1 for the different values of the applied field.

In phase I, a single-q structure with the moment along the fourfold axis and perpendicular to the magnetic propagation vector gives the best agreement between calculated and measured intensities:

$$\boldsymbol{M} = (0, 0, 1) \qquad \text{with } \boldsymbol{q} = (1/2, 1/2, 0).$$

This model leads to three magnetic domains corresponding to the three fourfold axes of the cubic structure. At zero field the three domains are equally distributed in the sample. As for the structure in phase II, the applied field tends to slightly distort the structure. Table 2

reports the results of the refinements in the collinear phase. The non-distorted structures associated with the two phases are drawn in figure 5. Among the 58 reflections collected at 4.8 and 28 K under 5 T, we have reported in table 3 the observed and calculated intensities for only some of them which best depict the intensity evolution between phases I and II. It was checked that the values of $M(T, H)$ deduced from these models are in good agreement with the ones observed in the magnetization curves.

5. Magnetic and magnetostrictive measurements in the dilute compound $(Tb_{0.02}Y_{0.98})In_3$

The thermal variation of the reciprocal first-order susceptibility is presented in figure 8. Its behaviour is isotropic. At high temperatures the susceptibility follows a Curie–Weiss law (see figure 6) and presents a Van Vleck behaviour below 5 K. This behaviour is confirmed by the measurements, performed down to 100 mK in the tetragonal symmetry, $H \parallel [001]$.

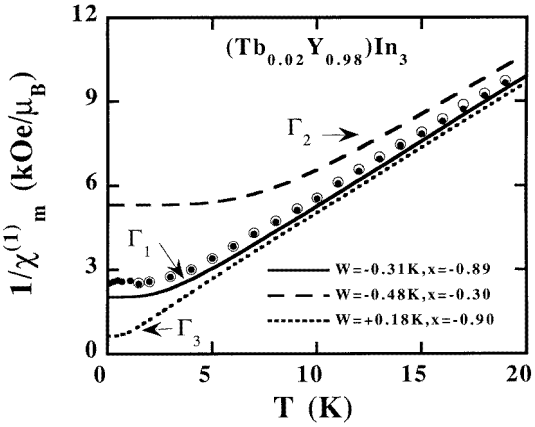

Figure 8. Thermal variation of the first-order magnetic susceptibility in $(Tb_{0.02}Y_{0.98})In_3$ at low temperatures. The experimental data are represented by full dots for $H \parallel [001]$ and open dots for $H \parallel [111]$. The fits for the different sets of CEF parameters are displayed by full, dashed and dotted lines.

The third-order magnetic susceptibilities determined for both the tetragonal and trigonal symmetries, corrected for the concentration, are shown in figure 9. They present a deep decrease below 5 K and remain negative down to the lowest temperatures. A significant anisotropy is observed for the third-order susceptibility between the tetragonal and trigonal symmetry. The low-temperature measurements in the tetragonal symmetry reveal a Van Vleck-type behaviour.

The thermal variation of $H/\sqrt{|\lambda_\parallel - \lambda_\perp|}$ was obtained with a fairly good precision up to 30 K (figure 10). For both symmetries, $H/\sqrt{|\lambda_\parallel - \lambda_\perp|}$ has a variation of Van Vleck-type below 5 K. At higher temperatures it increases linearly with the temperature. A larger slope is observed for the trigonal strains indicating a smaller rhombohedral length change.

The Van Vleck behaviour of the first-order magnetic susceptibility reveals that the CEF ground state of Tb ions is definitely non-magnetic. According to the Lea–Leask–Wolf diagrams [18], three non-magnetic ground states are possible, the Γ_1 and Γ_2 singlets or the Γ_3 doublet. In a previous work Czopnik *et al* [8] deduced a Γ_3 ground state for $TbIn_3$ with two possible sets of parameters: $W = 0.37$ K, $x = -0.83$ or $W = 0.27$ K, $x = -0.77$. Both

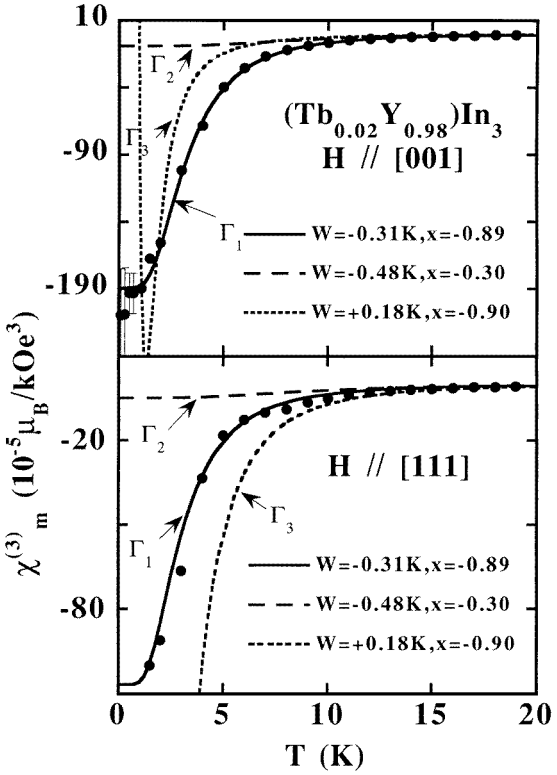

Figure 9. Experimental thermal variation of the third-order magnetic susceptibility in $(Tb_{0.02}Y_{0.98})In_3$ in both the tetragonal and trigonal symmetry (full dots). The lines represent the thermal variation calculated with the different sets of CEF parameters given in the figure.

sets lead to negative $A_4\langle r^4\rangle$ and $A_6\langle r^6\rangle$ parameters. A Γ_3 doublet ground state for the Tb^+ ion leads to non-zero $\langle\Gamma_{3_i}|O_2^0|\Gamma_{3_i}\rangle$ matrix elements, then the third-order magnetic susceptibility and the quadrupolar susceptibility should both diverge at zero Kelvin, at least for one symmetry. It turns out that such a ground state is inconsistent with the thermal variation observed experimentally for $H/\sqrt{|\lambda_\parallel - \lambda_\perp|}$. Indeed a Van Vleck behaviour of $H/\sqrt{|\lambda_\parallel - \lambda_\perp|}$, in both the tetragonal and trigonal symmetries, is only expected for a singlet ground state. This is confirmed by the calculations of the thermal variation of the first- and third-order susceptibilities and of $H/\sqrt{|\lambda_\parallel - \lambda_\perp|}$ performed with these two sets of parameters. In both cases, the calculations fail to fit simultaneously all the experimental variations.

Assuming a non-magnetic ground state, different sets of parameters in the Lea–Leask–Wolf diagrams [18] have been tested in order to describe simultaneously the thermal variation of the three CEF susceptibilities. The best agreement between calculations and experimental susceptibilities of $(Tb_{0.02}Y_{0.98})In_3$ was obtained for a Γ_1 ground state with $W = -0.31$ K and $x = -0.89$. This set corresponds to positive parameters, $A_4\langle r^4\rangle = 38.4$ K and $A_6\langle r^6\rangle = 3.3$ K. These parameters lead to a weak value of the CEF total spacing, which explains the difficulty of observing well resolved excitations by neutron spectroscopy. In table 4 we compare these values with those previously reported in $PrIn_3$ [14, 23] and in $NdIn_3$ [13]. The evolution of the $A_4\langle r^4\rangle$ and $A_6\langle r^6\rangle$ parameters from Pr to Tb appears very coherent.

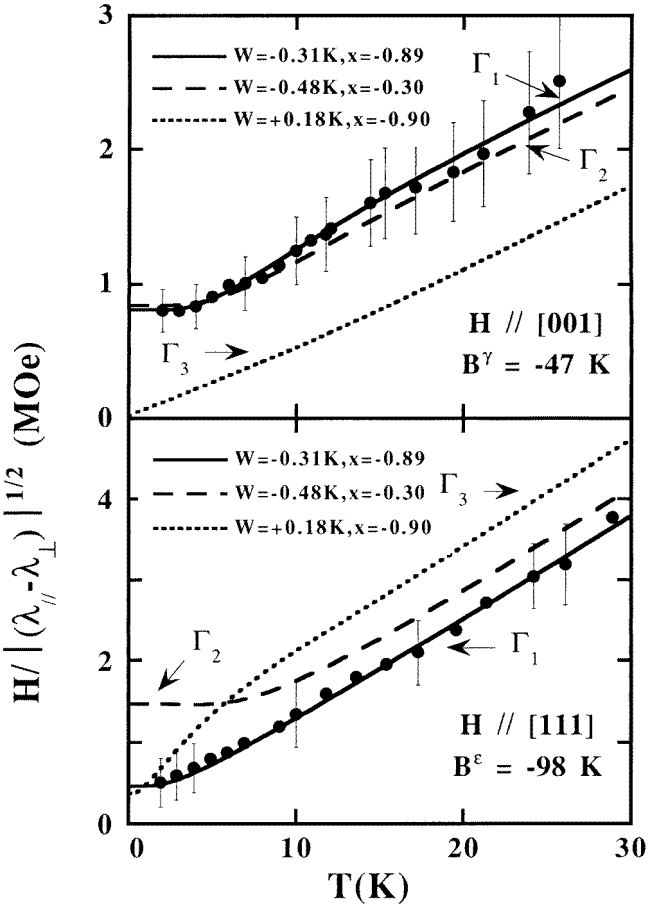

Figure 10. Experimental (full dots) and calculated (lines) thermal variation of $H/\sqrt{|\lambda_\parallel - \lambda_\perp|}$ in $(Tb_{0.02}Y_{0.98})In_3$ for the tetragonal and trigonal modes. Calculations have been performed using the CEF parameters and the values of the magnetoelastic coefficient B^μ given in the figure.

Table 4. CEF parameters and ground state in the $PrIn_3$, $NdIn_3$ and $(Tb_{0.02}Y_{0.98})In_3$ compounds.

Compound	$A_4\langle r^4\rangle$ (K)	$A_6\langle r^6\rangle$ (K)	Ground state
$PrIn_3$ [14]	32.1	12.3	Γ_1
$PrIn_3$ [23]	40.0	10.3	Γ_1
$NdIn_3$ [13]	30.5	6.8	$\Gamma_8^{(2)}$
$(Tb_{0.02}Y_{0.98})In_3$	38.4	3.3	Γ_1

The fits of the thermal variation of $H/\sqrt{|\lambda_\parallel - \lambda_\perp|}$ were performed using the background elastic constants deduced from the study of YIn_3, $C_0^\gamma = 4.5 \times 10^5$ K/atom and $C_0^\varepsilon = 5.5 \times 10^5$ K/atom. The values of the magnetoelastic coefficients which give the best fits are $B^\gamma = -47$ K and $B^\varepsilon = -98$ K for the tetragonal and trigonal mode respectively. Normalized by the second-order Stevens coefficient, the values, $B^\gamma/\alpha_J = +4600$ K/atom and $B^\varepsilon/\alpha_J = +9700$ K/atom, can be compared to those found in $NdIn_3$, $B^\gamma/\alpha_J = +1900$

or 900 K/atom and $B^{\varepsilon}/\alpha_J = +17\,000$ or 4400 K/atom. In the two compounds the magnetoelastic coefficients have the same sign as also in some other isomorphous compounds, like $CePb_3$ ($B^{\gamma}/\alpha_J = +1360$ K/atom and $B^{\varepsilon}/\alpha_J = +3400$ K/atom), $PrPb_3$ ($B^{\gamma}/\alpha_J = +2040$ K/atom and $B^{\varepsilon}/\alpha_J = +9100$ K/atom) or $TmGa_3$ ($B^{\gamma}/\alpha_J = +1700$ K/atom and $B^{\varepsilon}/\alpha_J = +7000$ K/atom) [1].

6. Description of the spontaneous phases in $TbIn_3$

Using the CEF parameters, $W = -0.31$ K, $x = -0.89$, deduced in section 5, we have calculated the thermal variation of the first-order magnetic susceptibility in $TbIn_3$. In this calculation only θ^*, the bilinear exchange coefficient, is adjusted ($\theta^* = nC$). The best agreement between the experimental data and the calculation is obtained for $\theta^* \approx -40$ K (see figure 6). Below 100 K, the experimental data deviate from the calculated Curie–Weiss law. According to the weak CEF splitting of the fundamental multiplet in $TbIn_3$, this deviation and also the larger experimental value of θ^*_{exp} ($\theta^*_{exp} = -56$ K) compared to the calculated one let us suppose that magnetic correlations affect the first-order magnetic susceptibility far above T_N. This also explains the difference between the theoretical effective moment and the experimental one.

A quantitative description of the magnetic properties of $TbIn_3$ has been undertaken in the ordered phase using the periodic-field method [24] extended to take into account the coexistence of both the bilinear and quadrupolar interactions [25]. In a first approach, taking into account only the CEF and the bilinear interactions, calculations with $W = -0.31$ K and $x = -0.89$ show that the free energy for a threefold easy magnetization direction remains, in the whole ordered domain, lower than the free energy for a fourfold axis. A threefold easy magnetization axis is in agreement with the spin arrangement in phase II. However to describe the change of the easy magnetization axis between phases I and II it is then necessary to introduce another type of interaction, for instance the quadrupolar ones. The existence of non-negligible quadrupolar interactions in $TbIn_3$ is supported by the stabilization of a triple-q structure at low temperatures. It is worth noting that the behaviour of $TbIn_3$ is very similar to those already observed in other cubic compounds like DyCu, DyAg or $TmGa_3$ where quadrupolar interactions strongly compete with dipolar ones.

With the quadrupolar Hamiltonian treated in the mean-field approximation ((8) and (9)), the total Hamiltonian (1) is then self-consistently diagonalized for each of the eight sites of the cubic magnetic cell. In a cubic symmetry the description of the quadrupolar coupling requires two dispersion curves, $K^{\gamma}(k)$ and $K^{\varepsilon}(k)$, associated with each quadrupolar irreducible representation $\Gamma_3(\gamma)$ and $\Gamma_5(\varepsilon)$. In addition to the crystal field parameters, the calculation requires the knowledge of (i) the Fourier transform of the bilinear exchange interactions, $J(0)$ and $J(k)$, (ii) the magnetoelastic coefficients, $B^{\gamma,\varepsilon}$ and (iii) the Fourier transform of the quadrupolar coupling constant, $K^{\gamma,\varepsilon}(k)$. In $TbIn_3$ the magnetic propagation vectors belong to the $\langle 1/2, 1/2, 0\rangle$ star, therefore in addition to $(0, 0, 0)$, only the $\langle 1/2, 1/2, 0\rangle$ quadrupolar propagation vectors are active. The occurrence of a second-order antiferromagnetic transition at T_N is determined by $J(1/2, 1/2, 0) = 1/\chi_0(T_N)$, where χ_0 is the CEF first-order magnetic susceptibility in the absence of any pair interactions. The value of $J(1/2, 1/2, 0)$ is obtained from the calculation of the CEF first-order susceptibility using the set of CEF parameters deduced in section 5. In the presence of bilinear interactions the experimental reciprocal first-order magnetic susceptibility obeys the relation $1/\chi^1_m(T) = 1/\chi_0(T) - n$ or using (4) $1/\chi^1_m(T) = 1/\chi_0(T) - J(0)/(g_J\mu_B)^2$. The value of $J(0)$ can then be deduced from the experimental value of $1/\chi^1_m(T_N) = 4.32$ T μ_B^{-1}. The values of $J(0)$ and $J(1/2, 1/2, 0)$ are given in table 4. $J(1/2, 1/2, 0) = 1.55$ T μ_B^{-1}

corresponds to a temperature of 32.8 K, a value close to T_N as result of the weak CEF splitting. $J(0) = -2.77$ T μ_B^{-1} corresponds to a temperature of -58.6 K. This experimental determination is affected by the short-range order effects, which have been shown to be important at least close to T_N, so a $J(0)$ value, smaller than the calculated bilinear exchange coefficient, is not surprising. This value better compares with that of $\theta^*_{exp} = -56$ K.

The magnetostriction measurements performed on the dilute sample give us the values of the magnetoelastic coefficients. Unfortunately in the absence of the same measurements in the paramagnetic range of $TbIn_3$, the values of $K^\gamma(0)$ and $K^\varepsilon(0)$ remain undetermined experimentally. The quadrupolar energy which intervenes in the total free energy for a [111] easy axis is related to the P_{ij} terms and the triple-q structure is stabilized as long as the quadrupolar coefficients satisfy the relation $K^\varepsilon(0) < K^\varepsilon(1/2, 1/2, 0)$. In low applied field the calculations show that $K^\varepsilon(0)$ is almost ineffective, so its value may be chosen arbitrarily provided it satisfies $K^\varepsilon(0) < K^\varepsilon(1/2, 1/2, 0)$. When the easy axis is a fourfold one, the quadrupolar energy contribution to the free energy is associated with the O_2^0 and O_2^2 terms and only single- or double-q structures can be stabilized. For a single-q structure (ferroquadrupolar interactions) the quadrupolar coefficients should satisfy $K^\gamma(0) > K^\gamma(1/2, 1/2, 0)$. Here also $K^\gamma(1/2, 1/2, 0)$ is inactive in zero field and its value is taken equal to zero in the calculations. Then the only two active parameters are $K^\varepsilon(1/2, 1/2, 0)$ and $K^\gamma(0)$. The value of $K^\varepsilon(1/2, 1/2, 0)$ was first adjusted in order to obtain the triple-q stabilization with a value of the magnetic moment at low temperature in agreement with the experimental one ($\mu_{Tb}(3\text{ K}) = 8.88 \pm 0.1\ \mu_B$ [21]). This condition is satisfied for values of $K^\varepsilon(1/2, 1/2, 0)$ in the range 12 to -12 mK. To stabilize the collinear structure in phase I, the second quadrupolar interaction coefficient $K^\gamma(0)$ is required. The $K^\gamma(0)$ value determines the transition temperature T_1. It was then adjusted to obtain the transition at the experimental value $T_1 = 26$ K. It turns out that the collinear structure can be stabilized only for negative values of $K^\varepsilon(1/2, 1/2, 0)$. For positive values of $K^\varepsilon(1/2, 1/2, 0)$ the triple-q structure is favoured in the whole ordered domain. The set of $K^\gamma(0)$ and $K^\varepsilon(1/2, 1/2, 0)$ values thus determined are given in table 5. In order to test the validity of this determination the specific heat and the thermal variation of the magnetization under an applied field of 0.4 T have been calculated. The calculations are compared in figures 11 and 12 to the experimental data. In both cases the agreement is fairly good.

Table 5. Dipolar and quadrupolar interaction coefficients used in the zero-field calculations.

$J(0)$ (T μ_B^{-1})	$J(1/2, 1/2, 0)$ (T μ_B^{-1})	$K^\gamma(0)$ (mK)	$K^\varepsilon(1/2, 1/2, 0)$ (mK)
-2.77	1.55	10.1	-10.0

It may be however pointed out that the set of quadrupolar coefficients introduced in the calculations is not the unique one. Indeed the lack of parastriction measurements in the paramagnetic phase in $TbIn_3$ does not allow us an estimation of the magnitude of $K^\gamma(0)$ and $K^\varepsilon(0)$. Nevertheless the values determined in this work can be compared with those found previously in $NdIn_3$. In $TbIn_3$ we calculate a total quadrupolar coefficient, $G^\gamma = (B^{\gamma^2}/C_0^\gamma) + K^\gamma(0) = 15$ mK; this value is quite consistent with the one deduced in $NdIn_3$, $G^\gamma = 12$ mK, from parastriction measurements in the paramagnetic range. Assuming antiferroquadrupolar interactions in $TbIn_3$ ($K^\varepsilon(0) < K^\varepsilon(1/2, 1/2, 0)$), G^ε should be smaller than 7 mK. This weak value for G^ε in $TbIn_3$ is also in agreement with $G^\varepsilon = 0$ in $NdIn_3$ and supports the validity of our determination.

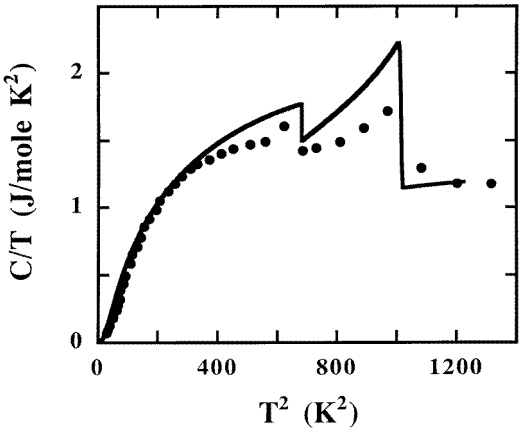

Figure 11. Full dots represent the experimental specific heat from [8]. The calculated specific heat is drawn in a full line.

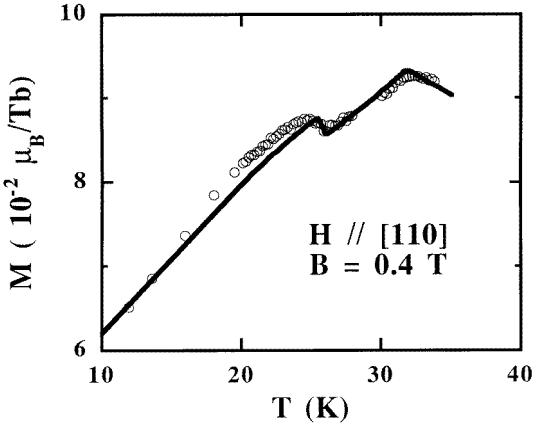

Figure 12. Thermal variation of the magnetization measured under 0.4 T with the magnetic field applied along the [110] axis (open dots). The full line represents the calculated thermal variation with the same conditions for direction and intensity of the magnetic field.

7. Conclusion

Neutron diffraction experiments on a single crystal and under magnetic field have allowed us to determine the actual spin arrangement in the two spontaneous phases of $TbIn_3$. The existence of antiferroquadrupolar interactions is strongly supported by the stabilization of a triple-q structure in the low-temperature magnetic phase. The present work has also demonstrated the possibility of using the CEF susceptibility formalism to have access to the crystal-field parameters at least in a dilute system. It turns out that in $TbIn_3$ these parameters are positive as in the light-rare-earth compounds of the series. This contradicts the statement of the sign change of the CEF parameters throughout the series reported in literature. The determination of the CEF parameters has been an essential step to further describe quantitatively the zero-field magnetic properties of $TbIn_3$. Within the mean-field approximation, the model used in this work takes into account the periodicity of both the

bilinear and quadrupolar interactions. The spontaneous phase transition is well reproduced by ferroquadrupolar γ and antiferroquadrupolar ε couplings of comparable intensity. This model was successfully developed by Amara and Morin [25] to describe the complex magnetic phase diagram in NdZn. Its application to $TbIn_3$ confirms its relevance to account for the magnetic properties in high-symmetry systems involving quadrupolar interactions.

Acknowledgments

We are grateful to C Paulsen and S Zherlytsin for their helpfulness during the magnetic measurements using the dilution refrigerator appliance. It is a pleasure to thank J Rouchy who has greatly contributed to the magnetostriction measurements.

References

[1] Morin P and Schmitt D 1990 *Ferromagnetic Materials* vol 5, ed K H J Buschow and E P Wohlfarth (Amsterdam: North-Holland) p 1
[2] Ball A R, Gignoux D, Schmitt D and Zhang F Y 1992 *J. Magn. Magn. Mater.* **104–107** 170
[3] Gignoux D, Morin P, Voiron J and Burlet P 1992 *J. Magn. Magn. Mater.* **104–107** 1262
[4] Kaneko T, Yosida H, Ohashi M and Abe S 1987 *J. Magn. Magn. Mater.* **70** 277
[5] Morin P and Schmitt D 1980 *J. Magn. Magn. Mater.* **21** 243
[6] Morin P, Rouchy J, Schmitt D and du Trémolet de Lacheisserie E 1990 *J. Magn. Magn. Mater.* **90/91** 105
[7] Morin P, Rouchy J, Yonenobu K, Yamagishi A and Date M 1989 *J. Magn. Magn. Mater.* **81** 247
[8] Czopnik A, De Boer F R, Veenhuizen P A, Gren B and Stalinski B 1990 *Physica* B **167** 49
[9] Czopnik A, Mädge H, Pott R and Stalinski B 1988 *Phys. Status Solidi* a **110** 601
[10] Amara M, Galéra R M, Morin P, Veres T and Burlet P 1994 *J. Magn. Magn. Mater.* **130** 127
[11] Amara M, Galéra R M, Morin P, Voiron J and Burlet P 1994 *J. Magn. Magn. Mater.* **131** 402
[12] Amara M, Galéra R M, Morin P, Voiron J and Burlet P 1995 *J. Magn. Magn. Mater.* **140–144** 1157
[13] Amara M, Morin P and Rouchy J 1994 *J. Magn. Magn. Mater.* **130** 115
[14] Lethuillier P and Chaussy J 1976 *J. Physique* **37** 123
[15] Lüthi B 1980 *J. Magn. Magn. Mater.* **15–18** 1
[16] Hog J and Touborg P 1975 *Phys. Rev.* B **11** 520
[17] Touborg P 1977 *Phys. Rev.* B **16** 1201
[18] Lea K R, Leask M J M and Wolf W P 1962 *J. Phys. Chem. Solids* **23** 1381
[19] Morin P, Rouchy J and Schmitt D 1988 *Phys. Rev.* B **37** 5401
[20] Creuzet G and Campbell I A 1982 *J. Magn. Magn. Mater.* **27** 221
[21] Galéra R M and Morin P 1992 *J. Magn. Magn. Mater.* **116** 159
[22] Amara M and Morin P 1996 *Physica* B **205** 379
[23] Groß W, Knorr K, Murani A P and Buschow K H J 1980 *Z. Phys.* B **37** 123
[24] Blanco J A, Gignoux D and Schmitt D 1991 *Phys. Rev.* B **43** 13 145
[25] Amara M and Morin P 1996 *Physica* B **222** 61